Hierarchical Silica Inverse Opals as a Catalyst Support for Asymmetric Molecular Heterogeneous Catalysis with Chiral Rh-diene Complexes

Max Deimling,[a] Shravan R. Kousik,[b] Karina Abitaev,[c] Wolfgang Frey,[a] Thomas Sottmann,[c] Kaloian Koynov,[d] Sabine Laschat,[a] and Petia Atanasova*[b]

The efficacy of heterogeneous catalysis relies heavily on diffusion and distribution of reactants within catalyst supports. However, the presence of confinement, essential for reaction selectivity, drastically slows down molecular transport. Here, macro-mesoporous silica inverse opal (SiO_2–IO) films were used as a model system to study the rather unexplored molecular infiltration behavior using a probe molecule resembling a catalyst via confocal laser scanning microscopy (CLSM). CLSM analysis revealed homogeneous tracer distribution in SiO_2–IO and attachment to both transport and mesopores. Bulk macro-mesoporous SiO_2–IO support was used for the attachment of mono- and bis-functionalized chiral Rh-diene complexes, and the catalytic activity and selectivity with respect to the support was studied. Lower enantioselectivity was observed with the bis-functionalized ligand due to ligand entanglement and reduced accessibility of the active site, while the mono-functionalized ligand gave an excellent enantioselectivity of 94%*ee* in the asymmetric 1,2-addition of triphenylboroxine to *N*-tosylimines and could be recycled up to three times.

Introduction

Semiconductor oxides with a hierarchical inverse opal (IO) structure are of potential interest for catalytic applications owing to their ordered structure in multiple length scales, open porosity, high surface area and thermal stability. With regard to catalysis, IOs offer a two-pronged advantage. Firstly, IOs of redox-active oxides like TiO_2, and CeO_2 can be used as nascent catalysts for organic transformations.[1,2] In addition, IOs of oxides like SiO_2, ZnO, Al_2O_3 and ZrO_2 can be used as mesoporous supports for the immobilization of catalytically active metal nanoparticles (NPs) and coordination complexes.[3–9] However, controlling the size and dispersion of NPs embedded within such porous structures has proved to be difficult.[10] The majority of studies on catalytic applications of IOs are focused on photo- and electrocatalysis, e.g. photocatalytic reduction of CO_2,[11] oxidation of CO,[12] degradation of organic materials for waste water treatment,[13–16] hydrogen production,[17] oxygen reduction,[18] and epoxidation of styrene.[19] However, pursuits have been made in recent years to expand the scope of IO-mediated catalysis. For instance, enzyme-containing SiO_2–IOs have been synthesized for potential application in enzyme catalysis.[20–22] Y. Jiang *et al.* have found improved catalytic performance and a remarkable reusability of lipase immobilized in hierarchically ordered macro-mesoporous silica.[23] Xin Fang *et al.* studied the catalytic activity and the factors affecting photoelectrogenesis in a model system consisting of photosystem II immobilized in macroporous indium tin oxide IOs.[24] IOs with immobilized catalysts, such as indenylzirconocene/MAO have been employed for ethylene polymerization.[25] In contrast, the immobilization of chiral transition metal catalysts in IOs and their application in asymmetric catalysis has not been reported.

As opposed to homogeneous catalysis, the efficiency of heterogeneous catalysis relies heavily on a number of physical factors such as diffusion, distribution, and infiltration depth of the reactant molecules. The use of tailor-made catalyst solid supports is critical to augment the efficiency of heterogeneous catalytic processes. It is therefore important to identify novel porous systems and study their pore architectures and transport properties using suitable physicochemical techniques. One distinct advantage of IOs is that their hierarchical porosity can

[a] M. Deimling, Dr. W. Frey, Prof. S. Laschat
Institute of Organic Chemistry
University of Stuttgart
Pfaffenwaldring 55
70569 Stuttgart (Germany)
[b] S. R. Kousik, Dr. P. Atanasova
Institute for Materials Science
University of Stuttgart
Heisenbergstraße 3
70569 Stuttgart (Germany)
E-mail: atanasova@imw.uni-stuttgart.de
[c] K. Abitaev, Prof. T. Sottmann
Institute of Physical Chemistry
University of Stuttgart
Pfaffenwaldring 55
70569 Stuttgart (Germany)
[d] Dr. K. Koynov
Max-Planck-Institute for Polymer Research
Ackermannweg 10
55128 Mainz (Germany)

Supporting information for this article is available on the WWW under https://doi.org/10.1002/cctc.202001997

This publication is part of a Special Collection on "Catalysis in Confined Spaces". Please check the ChemCatChem homepage for more articles in the collection.

be controlled by the number of different pore sizes and the range (micro-meso-macro) in which they appear in the porous structure. This in turn allows tuning the transport properties of IOs that are determined by a complex diffusion behavior.[26–28] For example, T. Cherdhirankorn *et al.*[26] studied the diffusion of small fluorescent tracers in macro-mesoporous SiO_2—IOs and identified three distinct diffusion modes: a) diffusion limited by the geometric constraints given by the macropores in the IO, b) slow diffusion inside the mesoporous matrix of the silica scaffold, and c) diffusion limited by adsorption on the pore walls. IOs are thus very useful model systems to study the transport properties of reactant molecules involved in heterogeneous catalytic reactions.

An emerging class in heterogeneous catalysis is molecular heterogeneous catalysis.[29] The catalyst molecules are tethered to the pore walls of the solid support either directly through an anchor group or the catalyst molecules are coupled to functionalized linker molecules already attached on the porous support via "click" reactions.[30,31] There are also a few examples in which the pore walls of macroporous materials were functionalized with organic molecules to enhance their surface properties. Prominently, organosilanes with different terminal functionalities were attached on macroporous TiO_2—IOs to optimize the wettability of the pore walls. This in turn led to an increase in contact area and improved the subsequent infiltration of a hole-transporting polymer. The existence of a self-assembled monolayer (SAM) of silanes on the pore walls was confirmed using XPS analysis and the changes observed in the photovoltaic performance of the resultant polymer-metal oxide hybrid solar cell.[32] In another approach to increase the wettability of macroporous polymer IOs, covalently bonded polyethylene glycol (PEG) groups were introduced on the pore walls of the IO via SAM formation with 2-[methoxy (polyethyleneoxy)propyl] trimethoxysilane.[33] The surface modification was verified via changes in the contact angle of the sample. Although the presence of SAM molecules was confirmed in these cases using XPS and contact angle measurements, there were no extensive studies performed to ascertain the localization and immobilization sites of the SAM molecules within the IO structure.

In addition to enhanced surfaced areas, achieved with the hierarchical structure of IOs, the presence of confined volumes in the mesopore range (2–50 nm) is of great importance to molecular heterogeneous catalysis.[34] There is a burgeoning need to identify a reliable method for mapping the positions of SAM and catalyst molecules immobilized on the pore walls of a support material. In this regard, confocal laser scanning microscopy (CLSM) is a powerful tool for visualizing the distribution of fluorescent species within porous materials. In recent years, the use of CLSM to monitor porous polymers and silica-containing polymeric dispersions has seen an upward surge.[35,36] CLSM was successfully employed to map the immunocapture of circulating tumor cells (CTCs) by a TiO_2—IO photonic crystal decorated with fluorescently labeled Fe_3O_4@C6@silane magnetic NPs.[37] Kubarev and coworkers[38] used super-resolution fluorescence microscopy to identify areas of enhanced reactivity in dealuminated mordenite zeolites. The technique was also used to monitor the immobilization of enzymatic catalysts on protein-based IOs.[39] Despite the advancements made in the use of CLSM to map porous architectures labeled with suitable fluorescent tracers, there have been little or no attempts to scrupulously determine the exact immobilization sites of organic molecules covalently bound to the pore walls of mesoporous oxide IOs.

Asymmetric transition-metal catalysis with chiral diene ligands has been extensively studied since the seminal discovery of chiral dienes as steering ligands.[40–43] However, immobilization of these catalysts has been much less explored. These studies utilized polystyrene (PS), PEG or NPs as supports and focused mostly on the efficient recycling of the catalyst.[44–50] Neither mesoporous silica materials nor SiO_2—IOs have been considered for this purpose. Furthermore, the role of the pore and confinement effects on asymmetric Rh-diene catalysis are virtually unknown. Therefore, to gain more insights into the distribution and localization of Rh-diene complexes in SiO_2—IOs, here, the penetration and the immobilization place of fluorescent probe molecules in mesoporous silica and hierarchical macro-mesoporous SiO_2—IO thin films, used as model systems, were studied via CLSM. As a probe molecule, we synthesized a fluorescent coumarin-functionalized silane. Coumarin dyes are well established for various applications,[51–56] and the coumarin labeled silanes are thought to be ideal probe molecules, because coumarins are of similar size and polarity as compared to the chiral diene ligands, so that their diffusion properties should correlate well with those of the Rh-diene complexes. Then, hierarchical macro-mesoporous SiO_2—IOs were used for the first-time as a catalyst support for chiral Rh-diene complexes, and their catalytic activity and selectivity with respect to the porous material was studied. As a catalytic model reaction, the Rh-diene-catalyzed 1,2-addition of phenylboroxine to *N*-tosylimines was chosen, because the corresponding homogeneous catalysis has been previously studied both experimentally and theoretically[41–43,57–60] and thus could serve as a benchmark for our novel solid catalyst.

Results and Discussion

In the first part of this work, the synthesis of a coumarin-functionalized silane is presented. The silane was subsequently used as a probe molecule to study the accessibility of the pores in macro-mesoporous SiO_2—IO films and mesoporous silica via CLSM. In the second part, chiral Rh-diene complexes were attached to a bulk macro-mesoporous SiO_2—IO support, functionalized with 3-azidopropyltriethoxysilane (AzPTES) linker through an azide-alkyne Huisgen cycloaddition reaction.[30,31] Finally, the asymmetric 1,2-addition of triphenylboroxine to *N*-tosylimines in heterogeneous conditions was studied.

Immobilization of fluorescent coumarin-functionalized silane in SiO_2–IO thin films and mesoporous silica

Synthesis of coumarin-functionalized silane: Care was taken to ensure that the synthesized fluorescent probe retained most of the defining characteristics of the actual ligand involved in the catalytic tests. Specifically, the fluorescent probe was functionalized with the same triethoxysilyl anchor group like the AzPTES linker. Given that the actual catalyst would be appended to the linker through a triazole-forming click reaction, the coumarin **5** was similarly clicked with AzPTES to obtain the fluorescent probe **6** (Scheme 1). Coumarin derivative **5** was prepared from 3-butyn-1-ol 1 via protection[61] of the terminal alkyne group followed by Jones oxidation[62] to obtain acid **3** as intermediate. The esterification and intramolecular ring closure were achieved by reaction of 4-bromosalicylaldehyde and iodine in the presence of triphenylphosphine and triethylamine.[63] Deprotection of coumarin derivative **4** was the key step in the linear synthesis pathway, because the reaction was only successful using a Olah's reagents (HF-pyridine complex)[64] instead of common reagents like TBAF[65] or K_2CO_3.[66] Coumarin derivative **6** was prepared via reaction with AzPTES in the presence of a soluble copper(I) complex.[67]

Assembly of silica porous materials and CLSM investigations: It has been shown that the diffusion of penetrants in the pores of IOs is a strongly restricted and rather complex process that depends on the considered length scale. Therefore, to enhance the transport of reactant molecules and facilitate catalytic reactions, at least bimodal (macro-mesoporous) IOs are needed as a catalyst solid support for heterogeneous catalysis. The big macropores should enable faster diffusion within the porous structure and together with the interconnecting (circular) pores should serve as transport pores. The mesopores in the pore walls on the other hand ensure a high surface area and confinement for stereoselective catalytic reactions. Thus, bimodal SiO_2–IOs thin films were prepared for the needs of the CLSM study by applying the co-assembly method. Sacrificial PS template particles with a diameter of 1 μm and 10 nm sized SiO_2 NPs were assembled in structured organic-inorganic hybrid films, as described in experimental part, and then, the template polymer beads were removed via pyrolysis. 1 μm sized PS particles were chosen as a template to ensure the formation of large transport pores in the inverse opal structure, and hence, better differentiation between the pores and the pore walls.

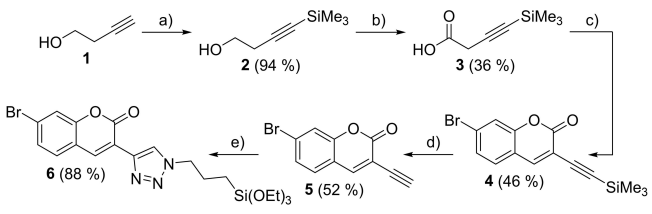

Scheme 1. Synthetic route towards the synthesis of **6**. Reagents and conditions: a) *n*BuLi, $Si(Me)_3Cl$, THF, −78 °C, 1 h; b) CrO_3, H_2SO_4, H_2O, acetone, 0 °C, 3 h; c) PPh_3, I_2, 4-bromo-2-hydroxybenzaldehyde, CH_2Cl_2, 0 °C→r.t., 16 h; d) HF·py, THF, −10 °C→r.t., 16 h; e) $Cu(PPh_3)_3Cl$ (10 mol%), NEt_3, AzPTES, THF, 60 °C, 6 h.

Different parameters like PS/SiO_2 ratio, PS and SiO_2 concentration in the particle suspension as well as the lifting speed were varied to tune the IO assembly conditions. The best conditions resulted in formation of films consisting of up to 5 PS layers. As commonly observed in oxide IOs inverse opals, the calcination step caused a crack formation in the porous structure separating highly crystalline areas from each other on microscopic level, but also within the pore walls as visible on the top view and cross-section SEM images in Figure 1.

In a bimodal porous system, an incoming guest molecule can occupy two different intercalation sites, namely the larger transport pores and the smaller mesopores on the pore walls. The choice of the intercalation site is predicated upon a complex interplay between steric and kinetic considerations and surface properties such as pore wettability and polarity. To gain first insights into infiltration behavior, probe molecules **6** were allowed to self-assemble in the macro-mesoporous structure of the SiO_2–O film, and their special distribution within the bimodal SiO_2–O was visualized via CLSM. The CLSM images in Figure 2 show the regular structure of the SiO_2–IO. The immobilization of the fluorescent probe molecules within the transport macropores can also be distinctly observed. The lower magnification image (Figure 2, left) gives an overview of the larger macroscopic superstructure of the IO, attesting the formation of cracks on the surface observed earlier with SEM analysis. A thorough investigation of the samples parallel to the film surface and along the Z-axis revealed the homogeneous distribution of the probe molecules in all the directions across the length of the SiO_2–IO film. Although the high magnification CLSM image (Figure 2, right) indicates the localization of the

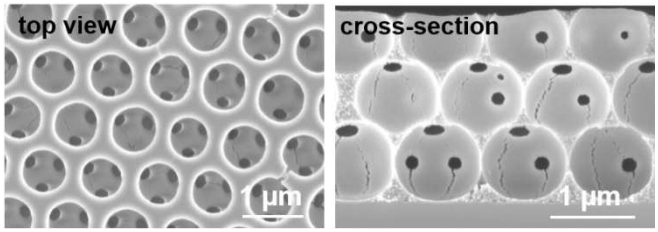

Figure 1. Top view and cross-section SEM images of a SiO_2–IO film obtained after calcination of colloidal crystal consisting of PS particles (d_{PS} = 1 μm) and SiO_2 NPs (d_{SiO2} = 10 nm).

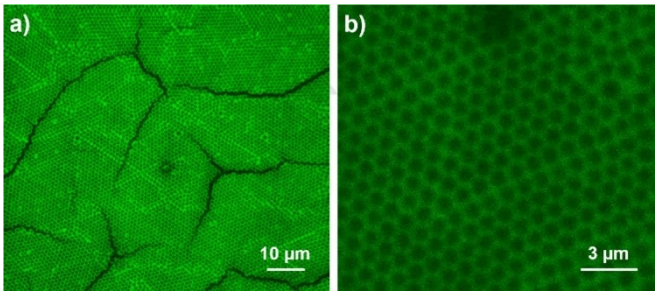

Figure 2. CLSM lower and higher magnification images of IOs with a transport pore diameter of around 1 μm assembled with silane probe molecules **6**.

fluorescent silane molecules in the silica scaffold, the diffraction-limited resolution of the confocal microscope (~300 nm in lateral and ~800 nm in normal direction) inhibits us from conclusively determining whether the fluorescent silane molecules are covalently bound to the mesopores or for reasons such as steric hindrance, choose to bind only to the larger transport pore walls.

To resolve this issue, the impact of the transport pores on the attachment of the silane molecules was excluded, and reference samples were prepared with only one type of pores, viz. mesopores. Both spin-coating and gravimetric sedimentation were used to assemble 10 nm sized SiO_2 NPs in mesoporous silica. The spin-coating treatment resulted in the formation of mesoporous silica films whose thicknesses were in the micrometer range, required for the CLSM measurements. However, the poor adhesion of the mesoporous silica films on the glass substrate made it difficult to efficiently immobilize the probe molecules on the silica surface. This impeded subsequent CLSM investigations. In contrast, mesoporous silica obtained using gravimetric sedimentation proved to be very useful for the immobilization of probe molecules. This method resulted in the formation of mesoporous silica granules with thicknesses running into several hundred micrometers. After self-assembly of the fluorescent silane **6**, the penetration depth of the probe was investigated by CLSM. Series of images (z-stacks) from optical sections, positioned at different distances from the cover glass/porous material interface were collected (see experimental part), and a 3D reconstruction of a part of the investigated reference was prepared as presented in Figure 3. The 3D image indicates that the probe molecules **6** attach not only on the silica surface, but also infiltrate deep into the mesoporous structure. The observed infiltration depth of the probe molecules (>25 μm) was far greater than the thickness of the pore walls of the SiO_2–IO studied earlier. With this, one can clearly confirm that in the case of SiO_2–IO films, the probe molecules not only covalently bond themselves to the larger transport pore walls but are also capable of intercalating and attaching themselves onto the mesopores.

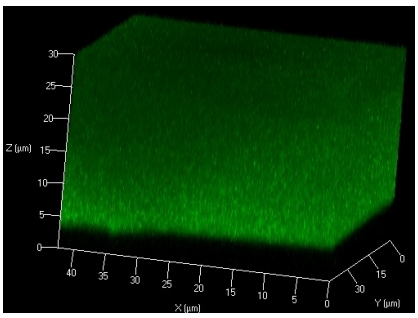

Figure 3. 3D CLSM image of a part of a reference mesoporous silica sample infused with immobilized fluorescent coumarin-functionalized silane **6**.

Molecular heterogeneous catalysis with SiO_2–IO solid support

Assembly and structural characterization of bulk macro-mesoporous SiO_2–IO catalyst support: Although the presence of an ordered, periodic structure is of great value to CLSM studies, seldom can IO films be directly used for catalytic reactions. The reason is that the protocol adopted for the assembly of IOs as highly structured thin films can hardly ensure the production of sufficient quantities for catalytic reactions. To mitigate the pitfalls associated with the poor scalability of the extant synthetic protocol, gravimetric sedimentation was explored to obtain hierarchically-ordered IOs in discernible quantities for catalysis. The solid support used to immobilize Rh-diene complexes for the asymmetric 1,2-addition reactions were prepared using this technique. Briefly, PS beads with a diameter of 370 nm and silica nanoparticles with a diameter of 10 nm were allowed to co-assemble and sediment under the influence of gravity. The structural features of the bimodal mesoporous silica material obtained after pyrolysis, were determined applying the complementary SEM, BET and SAXS methods. The SEM image in Figure 4a shows a cross-section of the SiO_2–IOs, where the presence of two differently structured domains is confirmed. The first type are well-ordered IOs domains (SiO_2–IO) consisting of macropores (transport pores with a diameter of 378±12 nm and circular pores with a diameter of 112±6 nm) and mesopores in the pore walls (Figure 4b). The other domains are made up of mesoporous silica without any transport pores. The presence of such transport pore-free domains between SiO_2–IO domains, might slow down molecular diffusion through the porous material during the catalytic reaction. However, despite multiple attempts the formation of mesoporous silica domains in the bulk SiO_2–IO could not be completely curtailed.

The bulk SiO_2–IO material was subsequently characterized using N_2 adsorption-desorption measurements. The obtained isotherm is shown in Figure 5a. The isotherm follows type IV(a) kinetics with an H1 hysteresis loop and a saturation plateau at high values of P/P_o. This indicates the presence of an ordered mesoporous structure with a uniform distribution of mesopores. The surface area of the porous material was calculated using the Brunauer-Emmett-Teller (BET) equation. The mesopore diameters were obtained by applying the Barrett-Joyner-Halenda (BJH) equation to the desorption branch. The BET surface area of the SiO_2–IO is 168.38 m^2/g. From the BJH pore-size distribution plot (Figure 5b), the diameter of the mesopores

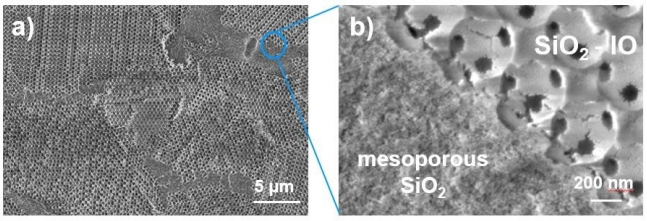

Figure 4. a) A cross-section SEM image of bulk SiO_2–IOs. It consists of well-structured IOs domains (SiO_2–IO) with big transport and circular macropores and mesopores. Additionally, single mesoporous silica domains without transport pores are also visible. b) Cross-section SEM image of the bulk

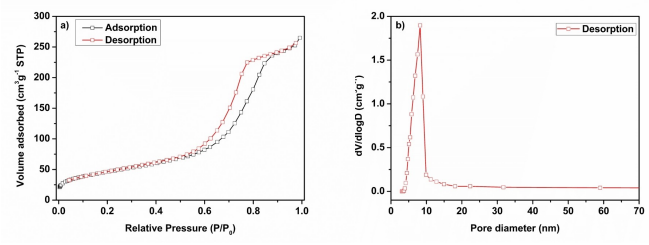

Figure 5. a) N_2 adsorption-desorption isotherm of the SiO_2–IO bulk material. b) Pore-size distribution calculated from the desorption branch.

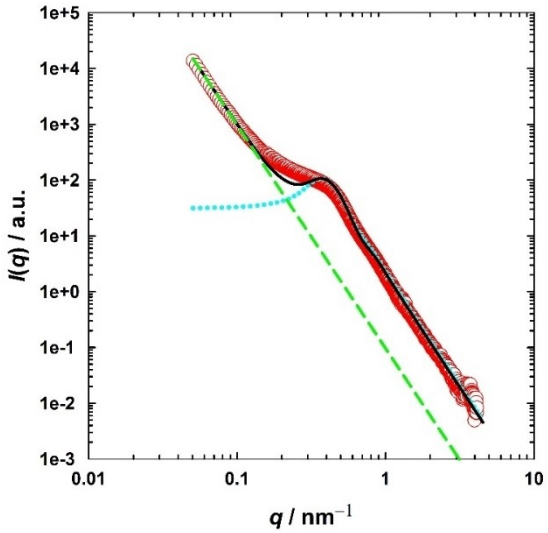

Figure 6. SAXS curve of the SiO_2–IO bulk material. The solid line illustrates the combined fits for the macropores (dashed line) and SiO_2 NPs (dotted line) scattering contributions.

was determined to be ~8.2 nm, which is bigger compared to pore diameters of $d_t \approx 4$ nm and $d_o = 7$ nm expected for tetrahedral (t) and octahedral (o) voids in face-centered cubic (fcc) packing, respectively.[68] The diameter of the transport pores is too large to be quantified by this technique.

In order to obtain quantitative information on the structural length scales of the bulk SiO_2–IO, small-angle X-ray scattering (SAXS) was used. The goal was to determine not only the size and polydispersity of the silica particles, but also their packing in the IO as well as the contributions of macropores and mesopores (between the silica particles) to the surface area. The obtained SAXS curve is shown in Figure 6 in a double logarithmic plot of the scattering intensity $I(q)$ as a function of the absolute value of the scattering vector q. The intensity is given in arbitrary units, since the SiO_2 powder was not homogeneously packed in the measurement cell. Three distinct features of the scattering curve are observed: At low q-values ($q \leq 0.1$), the scattering intensity, which originates mainly from the large macroporous transport pores, decreases with a steep q^{-4} decay. This decrease is followed by a broad scattering shoulder around $q \approx 0.4$ nm^{-1} and a slight dent around $q \approx 1$ nm^{-1}. While the position of the shoulder is mainly related to the packing order, as well as the average distance of the SiO_2 NPs, the position and distinctness of the dent allows for the determination of the size and polydispersity of the SiO_2 NPs. At higher q-values the scattering is characterized by another q^{-4} decay allowing in principle for determination of the surface area of the mesopores.

To describe the scattering curve, the scattering contributions of the macropores as well as the scattering of the SiO_2 NPs were considered. Large parts of the structure and form factor contributions of the macropores, expected to occur at very small q-values ($q = 2\pi/d < 0.005$ nm^{-1}), could not be recorded due to limitation in the q-range. However, analyzing the q^{-4} decay at low q using Porod's q^{-4} decay[69] allowed to determine the relative contribution of the macropore surface. From the analysis of the intermediate and large q-regime (for details see experimental part), a silica particle size of $d_{SiO2} = 11.4$ nm $\pm$ 3.4 nm and polydispersity of $p_{SiO2} = 0.29 \pm 0.03$ was obtained. These values are in quantitative agreement with the average silica particle size given by the supplier ($d_{SiO2} = 10$ nm). Furthermore, the volume fraction of SiO_2 NPs on the mesoscopic scale was found to be $\Phi_{SiO2} = 0.45 \pm 0.05$, and thus, a volume fraction of the mesopores between the SiO_2 NPs of $\Phi_{mesopores} = 0.55$. This value is considerably higher than the free volume of a fcc packing ($\Phi = 0.26$), which can be assigned to an unordered packing of the polydisperse silica particles. A comparison of the two scattering contributions (macropores and SiO_2 NPs) at high q allows for the determination of their relative contributions to the overall surface area of the bulk SiO_2–IO material. Performing this analysis at three different sample positions, we obtained that the contribution of the mesopores to the overall surface area is a factor of 20 ± 2 larger than the contribution of the much bigger macropores. Assuming that the pore architecture of the bulk materials consists exclusively of SiO_2–IO domains, the SiO_2 NPs contribution should only be a factor of 10 larger. From this, we conclude that the recorded scattering curve originate from sample positions with both SiO_2–IO and mesoporous SiO_2 domains.

Synthesis of chiral diene ligands: In order to investigate the influence of the symmetry, steric bulk, and rigidity of bicyclo [3.3.0]octadienes in the macro-mesoporous SiO_2–IO support on the performance in rhodium catalysis, two derivatives were synthesized in a one-pot synthesis (Figure 7).

The synthesis of chiral bicyclo[3.3.0]octadienes **L1** and **L2** started from the known bis-enoltriflate[70] **7** with a previously published Suzuki coupling[71] using an equimolar mixture of phenylboronic acid and 4-hydroxyphenylboronic acid in the presence of 10 mol% $Pd(PPh_3)_4$ to yield a stochiometric mixture of diphenyldiene **L3** (23%), di(4-hydroxyphenyl)diene **9** (15%) and mono(4-hydroxyphenyl)diene **8** (41%) (Scheme 2). Notably, no waste is generated since both phenolic dienes **8** and **9** could be functionalized in a second run, while the diphenyldiene **L3** serves perfectly as a benchmark ligand with broad applications.[72–77] Williamson etherification of **8** with 1.1 equiv. 6-chloro-1-hexyne in the presence of Cs_2CO_3 in DMSO gave the mono-functionalized alkyne **L1** in a yield of 53%. Di(4-hydroxyphenyl)diene **9** was reacted under identical conditions

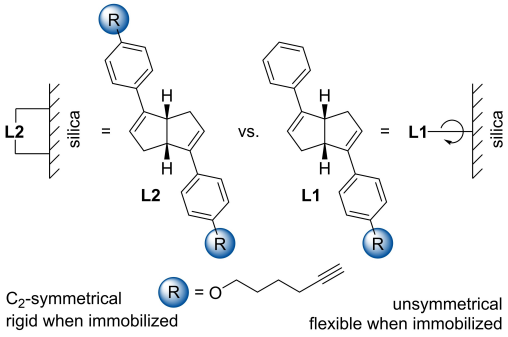

Figure 7. Overview of prepared symmetrical and unsymmetrical bicyclo[3.3.0]octadienes **L1** and **L2** and their proposed binding situation in the macro-mesoporous SiO_2–IO.

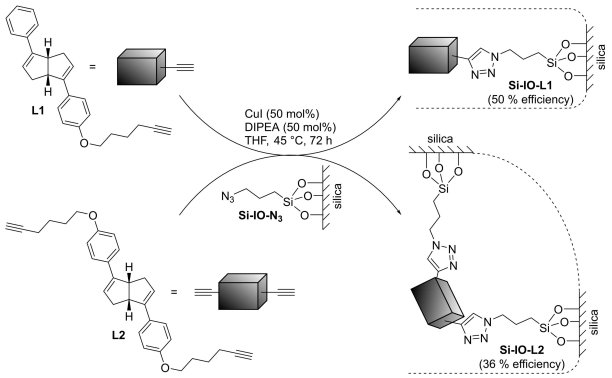

Scheme 3. Immobilization of alkyne-functionalized diene ligands **L1** and **L2** on 3-azidopropyl-functionalized SiO_2–IOs via CuAAC.

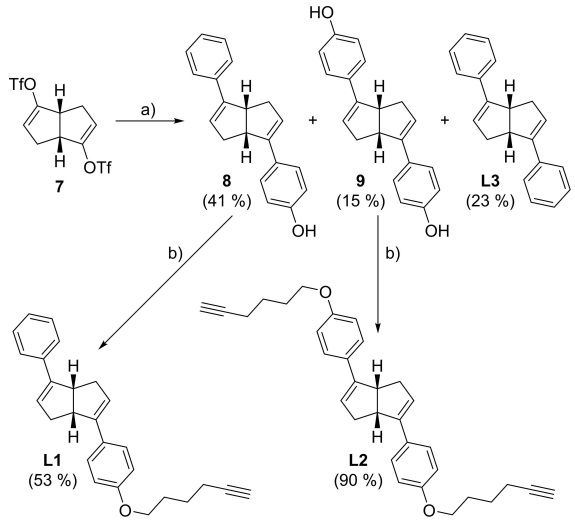

Scheme 2. Synthesis of alkyne-functionalized bicyclo[3.3.0]octadienes **L1** and **L2**. Reagents and conditions: a) $Pd(PPh_3)_4$ (10 mol%), 4-OH-$C_6H_4B(OH)_2$, $C_6H_5B(OH)_2$, $NaHCO_{3(aq)}$, DME, 100 °C, 16 h; b) Cs_2CO_3, KI, 6-chloro-1-hexyne, DMSO, 90 °C, 16 h.

using 2.2 equiv. of 6-chloro-1-hexyne to yield the bis-functionalized alkyne **L2** in 90%.

Immobilization of chiral bicyclo[3.3.0]octadienes in bulk SiO_2–IOs: In the next step, the SiO_2–IOs support was functionalized with AzPTES linker. The elemental analysis of the azide-functionalized porous silica has shown attachment of 0.365 mmol/g linker molecules with azide-terminal groups on the silica surface. The synthesized alkyne-functionalized dienes **L1** and **L2** were then immobilized on the silica support via an azide-alkyne Huisgen cycloaddition in the presence of 50 mol% CuI (with respect to alkyne groups) (Scheme 3). The mono-functionalized diene **L1** could be immobilized in an efficiency of 50% (0.19 mmol/g), while the bis-functionalized diene **L2** could be immobilized in an efficiency of 36% (0.07 mmol/g). Click reaction efficiencies were determined via ^{1}H-NMR spectroscopy from the combined washing solutions with respect to unreacted alkyne using mesitylene as an external standard. Therefore, please also note that in the case of bis-functionalized diene **L2** no differentiation was possible between mono- and double-clicked diene ligand since the intensity of ν(C–H) of unreacted alkynes are below the detection limit of the IR spectrometer. We assume that lower click efficiency for the bis-functionalized diene **L2** is caused by a combination of increased steric bulk and an entanglement of functional groups inside the pores due to the flexible alkyl spacers. Since the azide-terminated silane AzPTES presumably attached on both the transport pore walls and in mesopores of the SiO_2–IO support, it is expected that the diene ligands **Si**–**IO**–**L1** and **Si**–**IO**–**L2** are also located inside and outside the mesopores. It should be noted, that other methods for immobilization on silica, such as $CuSO_4$/NaAsc[78] in CH_2Cl_2/H_2O (3:1) gave conversions below 5%, while another method of CuI and DIPEA in MeCN[79] failed completely due to insolubility of diene ligands **L1** and **L2**.

The SEM analysis of the pore structure of **Si**–**IO**–**L1** after immobilization of the ligand **L1** revealed that the overall pore structure did not change, while small pieces of silica support were distributed over the porous network presumably due to abrasion caused by mechanical stirring (Figure S1a,b).

Rh-catalyzed asymmetric 1,2-additions: Bicyclo[3.3.0] octadiene ligands **L1**–**L3** and their immobilized forms **Si**–**IO**–**L1** and **Si**–**IO**–**L2** were employed in Rh-catalyzed asymmetric 1,2-additions of triphenylboroxine **11** to *N*-(4-chloro)tosylimine **10** (table 1). In order to study the influence of a triazole moiety on the catalysis, mono-functionalized diene **L1** was reacted with benzylazide in a CuAAC in the presence of 10 mol% $Cu(PPh_3)_3Cl$ to yield **L4** in 38%. On the other hand, phenylacetylene was clicked to azide-functionalized silica (**Si**–**IO**–$\mathbf{N_3}$) in the presence of 50 mol% CuI to give **Si**–**IO**–**Ph** in an efficiency of 96% (0.36 mmol/g) (Scheme 4).

The reaction using only the rhodium precursor $[Rh(C_2H_4)_2Cl]_2$ resulted in the formation of 22% racemic product **12** (entry 1). As benchmark systems, $[Rh(cod)Cl]_2$ and $[Rh(C_2H_4)_2Cl]_2$/diphenyl-diene **L3** were used under homogeneous conditions. In the former case, 58% of racemic product **12** were obtained (entry 2), while in the latter case, product **12** was formed exclusively in a yield of 98% with 96%*ee* (entry 3).

In a series of experiments, various sources of silica differing in morphology and functionalization were used (entries 5–10)

Table 1. Rh-catalyzed 1,2-addition of triphenylboroxine **11** to *N*-tosylimine **10** in the presence of various silica sources, synthesized diene ligands **L1**–**L4** and their immobilized forms **Si**–**IO**–**L1** and **Si**–**IO**–**L2**.[a]

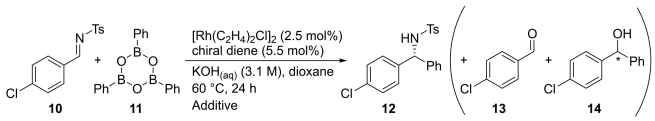

Entry	Ligand	Additive[b]	Conv. [%]	NMR yield [%][c] 13	14[f]	12	Yield [%][d]	*ee* [%] (*R*)[e]
1	–	–	78	53	1	22	n.d.	n.d.
2	cod[g]	–	64	4	1	59	58	0
3	**L3**	–	>99	0	1	99	98	96
4	**L3**	$CuSO_4 \cdot 5H_2O$	>99	0	0	99	98	96
5	–	Sand	92	62	5	25	n.d.	n.d.
6	–	Silica gel	71	4	3	65	n.d.	n.d.
7	–	**Si**–**IO**	>99	2	5	93	n.d.	n.d.
8	–	**Si**–**IO**–$\mathbf{N_3}$	>99	2	5	93	83	0
9	–	**Si**–**IO**–$\mathbf{N_3}$[h]	95	95	0	0	–	–
10	–	**Si**–**IO**–**Ph**	76	12	0	64	63	0
11	**L2**	–	97	4	29	63	56	95
12	**Si**–**IO**–**L2**	–	45	31	5	9	9[i]	44
13	**L1**	–	>99	0	6	94	93	95
14	**L1**	**Si**–**IO**–$\mathbf{N_3}$	>99	0	9	91	91	93
15	**L4**	–	88	9	9	70	62	97
16	**Si**–**IO**–**L1**	–	81	17	15	49	47	94

[a] Reaction conditions: Imine **10** (0.20 mmol), triphenylboroxine **11** (0.24 mmol), diene ligand (5.5 mol%), Rh (2.5 mol%), dioxane (1.6 mL), aqueous KOH (13 μL, 3.1 M), 60 °C, 24 h [b] 5.5 mol% related to functional groups or 10.0 mg were added. [c] Determined by ^{1}H-NMR spectroscopy using mesitylene as an external standard. [d] Isolated yields. [e] Determined by HPLC analysis on a chiral OD–H column. [f] No isolation attempts were made and no *ee* was determined. [g] $[Rh(cod)Cl]_2$ was used. [h] No Rh was added. [i] No pure product could be isolated. n.d. = not determined.

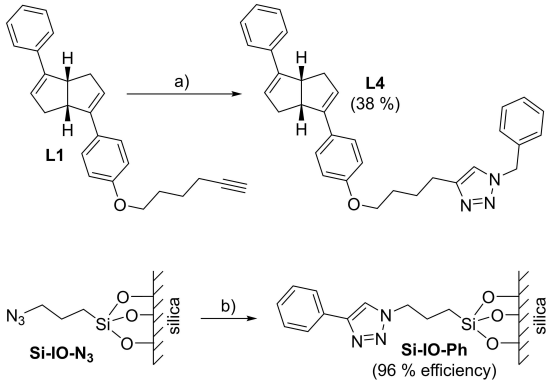

Scheme 4. Synthesis of diene ligand **L4** carrying a triazole moiety and reaction of azide-functionalized silica inverse opals (**Si**–**IO**–$\mathbf{N_3}$) with phenylacetylene to give **Si**–**IO**–**Ph**. Reagents and conditions: a) $Cu(PPh_3)_3Cl$ (10 mol%), BnN_3, NEt_3, THF, 60 °C, 16 h; b) CuI (50 mol%), phenylacetylene, DIPEA, THF, 45 °C, 72 h.

to study the influence of porous silica on the chemoselectivity. These reactions provided racemic products due to the absence of chiral diene ligands **L1**, **L2**. While commercially available amorphous sand gave similar results compared to the background reaction, (25%, entry 5), commercial silica gel (6 nm pore size) gave a higher yield of product **12** (65%, entry 6. Unfunctionalized (**Si**–**IO**) and azide-functionalized macro-mesoporous SiO_2–O (**Si**–**IO**–$\mathbf{N_3}$) both resulted in even higher yields of 93% (entries 7, 8). Please note that the azide-functionalized SiO_2–O support without rhodium precursor was not able to form the product **12**, and mainly the hydrolysis product **13** was observed (entry 9). These results indicate that the silica source has a significant influence on the catalysis. A higher porosity of the silica support enhanced the chemoselectivity towards the desired product **12**. Additionally, when phenyl-functionalized silica **Si**–**IO**–**Ph** was used (entry 10), the yield (63%) was similar to silica gel (entry 6), but lower as compared to **Si**–**IO**–$\mathbf{N_3}$ (entry 8). This is probably due to increased steric bulk inside the pores and therefore an increased diffusion limitation of substrates. The high degree of occupancy of azides with phenyl groups also led to much more hydrophobic pore walls, which on the other hand might interfere with the active rhodium complex formation with aqueous KOH.

In the next series of experiments, the synthesized alkyne-functionalized dienes **L1** and **L2** and their immobilized forms **Si**–**IO**–**L1** and **Si**–**IO**–**L2** were studied. The bis-functionalized diene ligand **L2** yielded product **12** under homogenous conditions in 56% with a high enantioselectivity (95%*ee*) together with the alcohol byproduct **14** in 29% (entry 11). In contrast, upon employing **Si**–**IO**–**L2** only small amounts of product **12** were formed (9%, 44%*ee*), while the amount of hydrolysis product **13** (31%) increased (entry 12). Presumably, unreacted alkyne groups from the immobilization reaction and entanglement of ligands inside the pores interfered with the diffusion of substrates. The moderate enantioselectivity indicates problems with the accessibility of catalytically active sites of the rigid Rh/**Si**–**IO**–**L2**-complex inside the pores. Residual copper on the silica surface as a leftover from the ligand immobilization can be excluded as a problem since it did not influence the reaction at all (entry 4).

In contrast, mono-functionalized diene **L1** performed surprisingly well under homogenous conditions (entry 13) with a very high product yield of 94% with excellent 95%*ee*, despite the absence of the C_2-symmetry.[80] Addition of azide-functionalized silica **Si**–**IO**–$\mathbf{N_3}$ did not disturb the homogeneous reaction, only the enantioselectivity decreased marginally to 93%*ee* (entry 14). Triazole carrying diene ligand **L4** was also used under homogenous conditions (entry 15). The triazole moiety appears to influence the reaction, because conversion of starting materials and isolated product yield dropped to 62%, while the enantioselectivity slightly increased to 97%*ee*. The lowered yield of product **12** can be explained by a folding of the flexible alkyl spacer and coordination of the triazole to the rhodium under basic conditions.[81] When the immobilized diene **Si**–**IO**–**L1** was employed, product **12** was obtained with a high enantioselectivity (94%*ee*) albeit moderate yield (47%) (entry 16). With regard to conversion and byproduct formation, there still seem to be diffusion limitations, however the more flexible Rh/**Si**–**IO**–**L1**-complex circumvented the problems of ligand entanglement and accessibility of the active site. The rhodium/triazole coordination could possibly be prevented by using shorter or more rigid spacers. Compared to bis-functionalized **Si**–**IO**–**L2**, yields could be significantly increased, while keeping the enantioselectivity at the same excellent level as under homogenous conditions.

Recycling experiments: Immobilized diene ligand **Si**–**IO**–**L1** was employed in a series of 1,2-addition reactions of triphenylboroxine **11** to *N*-tosylimine **10** to test catalyst recycling (table 2). The catalyst could be recovered by simple centrifugation, subsequent washing with dioxane and dioxane/H_2O and drying *in vacuo*.

The 1st cycle gave identical results than before (table 1, entry 16), however no product **12** could be observed after the 2nd cycle. Only starting material **10** and hydrolysis product **13** were found. ICP-OES analysis of the silica support after the 2nd cycle revealed a leeching of 32.6% of the initially added amount of rhodium, which was also indicated by a reddish washing solution after each of the two cycles. Thus, the silica support recovered after the 2nd run was treated with additional 2.5 mol% $[Rh(C_2H_4)_2Cl]_2$ and the catalytic 1,2-addition was performed again. In the 3rd cycle, product formation was indeed observed with slightly lower yield (36%) and enantioselectivity (89%*ee*) as compared to the first run. In the 4th and 5th run NMR yields decreased further to 28% and 15% respectively, while the *ee* values remained at 78%*ee*. In order to study possible leeching of the immobilized diene ligands, washing solutions were investigated after each of the first three cycles via mass spectrometry (EI and ESI). No hints for a ligand leaching could be found since all mass peaks could be assigned to the reagents **10** and **11** and products **12**–**14** of the catalytic reaction. The majority of the rhodium seems to be deactivated by deposition on the silica surface, because the immobilized diene ligands were still accessible for fresh Rh precursor as indicated by the enantioselective formation of **12**. The required recharging with Rh precursor and the observed decrease of catalytic activity and enantioselectivity after a few runs is in good agreement with previous observations by Yang and Xu[50] employing polymer-bound bicyclo[3.3.0]octadienes in Rh-catalyzed 1,4-additions. The impact of the catalytic reaction on the pore diameter of **Si**–**IO**–**L1** was ascertained from BET analysis (Figure S2). Compared to the untreated silica support, a reduction in the pore diameter was observed after 5 catalytic cycles. The pore size distribution showed two dominant peaks at ~3.7 and ~5.4 nm. In addition, SEM investigations of **Si**–**IO**–**L1** after the 1st and 5th catalytic runs showed the appearance of spherical nanoparticles on the pore walls of the macropores (Figure S1c–f). A potential reason for deactivation might be pore blocking by Rh boronate precipitates in agreement with recent calculations of the catalytic cycle.[60]

Conclusion

In summary, bimodal macro-mesoporous SiO_2–IO thin films and their corresponding mesoporous silica references were fabricated and used as model systems to investigate the spatial distribution and localization of attachment sites of catalyst-resembling probe molecules via CLSM. For this study, a coumarin-based fluorescent probe was synthesized and infiltrated into the porous materials. The CLSM analysis showed that the fluorescent probe molecules could be uniformly distributed within the transport macropores of the SiO_2–IOs, and localized in the silica scaffold, bind to the larger transport pore walls. Further investigation on the probe infiltration within

Table 2. Recovery and reuse of immobilized diene **Si**–**IO**–**L1** in multiple cycles of the Rh-catalyzed 1,2-addition of triphenylboroxine **11** to *N*-tosylimine **10**.[a]

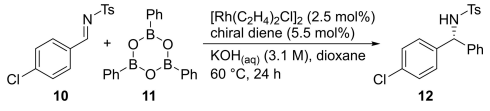

Catalytic cycle	1st	2nd	3rd [b]	4th [b]	5th [b]
NMR Yield [%][c]	50	0	38	28	15
Yield [%][d]	48	–	36	24	(10)[d]
ee [%] (*R*)[e]	94	–	89	78	78

[a] Reaction conditions: Imine **10** (0.10 mmol), triphenylboroxine **11** (0.12 mmol), **Si**–**IO**–**L1** (5.5 mol%), $[Rh(C_2H_4)_2Cl]_2$ (2.5 mol%), dioxane (1 mL), aqueous KOH (7 µL, 3.1 M), 60 °C, 24 h [b] Fresh $[Rh(C_2H_4)_2Cl]_2$ (2.5 mol%) was added. [b] Determined by ^{1}H-NMR spectroscopy using mesitylene as an external standard. [c] Isolated yields. [d] No pure product could be isolated. [e] Determined by HPLC analysis on a chiral OD–H column.

transport pore-free reference samples revealed that the silane molecules could infiltrate deep inside the mesoporous silica and covalently bind to the mesopores. Owing to their hierarchical structure and enhanced surface area, SiO_2–IOs were chosen and used for the first time as a catalyst support for Rh-catalyzed asymmetric 1,2-addition reactions. Thus, macro-mesoporous SiO_2–IO material was assembled in bulk through gravimetric sedimentation of 370 nm sized PS sacrificial particles and 10 nm sized SiO_2 NPs. The structure of the porous material was characterized using SEM, BET and SAXS measurements. Two distinct structural domains were confirmed via SEM, namely, mesoporous silica domains and well-ordered IO domains consisting of transport macropores with a pore diameter of 378 ± 12 nm, circular pores with a diameter of 112 ± 6 nm and mesopores in the pore walls. From BET measurements, the diameter of the mesopores was ascertained to be 8.2 nm. The analysis of the SAXS-curve revealed that the surface area of the assembled SiO_2 NPs with calculated diameter of $d_{SiO2} = 11.4\ nm \pm 3.4\ nm$ is 20 times larger than the surface area of the macropores. The broadness of the interaction peak clearly indicates a disordered packing of SiO_2 NPs explaining why the 8.2 nm mesopores are larger than expected from fcc packing. The macro-mesoporous SiO_2–IO support was functionalized with AzPTES linker, and subsequently chiral diene ligands **L1**, **L2** carrying one or two alkynyl arms were immobilized via CuAAC click reaction inside the pores of SiO_2–O to yield **Si**–**IO**–**L1, Si**–**IO**–**L2**, respectively. Large differences in the catalytic properties were observed for these SiO_2–O materials. While the bis-functionalized catalyst Rh/**Si**–**IO**–**L2** gave poor yield (9%) and only moderate enantioselectivity (44%*ee*) in the Rh-catalyzed 1,2-addition of triphenylboroxine to *N*-tosylimine, the corresponding mono-functionalized catalyst Rh/**Si**–**IO**–**L1** provided the product in increased yield (47%) and excellent enantioselectivity (94%*ee*). This outcome could be rationalized by reduced entanglement and better accessibility of the active site in the pores for **Si**–**IO**–**L1** as compared to **Si**–**IO**–**L2**. The immobilized diene ligand **Si**–**IO**–**L1** could be recycled up to three times with a moderate loss in enantioselectivity. More insight is needed to improve the yields inside the pores as compared to the homogeneous conditions. Nevertheless, these results have demonstrated the potential of SiO_2–IOs for asymmetric catalysis paving the way for other catalytic reactions.

Experimental Section

Assembly of SiO_2–IO thin films for CLSM: Round microscope glass slides (Paul Marienfeld GmbH, Germany) with diameter of 25 mm and thickness of 170 μm were used as substrates for assembly of SiO_2–IOs films. The glass slides were previously cleaned to get a hydrophilic surface applying the following procedure: 10 min sonication in ultrapure water, 10 min sonication in ethanol/acetone (1:1, v/v), 10 min O_2 plasma treatment (30 W) and 10 min sonication in ultrapure water. After each sonication step, the substrates were washed 10 times with the corresponding solvent and dried under nitrogen stream. One side of the slides was covered with protecting foil. Then, a glass slide was placed vertically in a suspension consisting of 200 μL (50 wt%) PS particles with a diameter of 1 μm, 20 μL (30 wt%, PlasmaChem) SiO_2 NPs with a diameter of 10 nm and 1780 μL water. The glass substrate was lifted out forming at the liquid-solid-air contact line a mixed colloidal crystal. Typical parameters for the assembly ranged from 21 to 23 °C environmental temperature, 40%–45% RH environmental humidity, and the lifting speed was 0.02 mm/min. After removal of the protecting foil, the PS template particles were removed by pyrolysis in air at 450 °C for 3 hours (1 °C/min).

The reference mesoporous silica thin films were prepared via gravimetrical sedimentation or spin coating of SiO_2 NPs with a diameter of 10 nm on plasma cleaned round microscope glass slides applying two deposition cycles. Each spin coating cycle consisted of the following steps: 200 μL (30 wt%) SiO_2 suspension was drop cast on a plasma-cleaned round microscope glass slide and spin coated for 60 s at 200 rpm, 120 s at 1000 rpm and 10 s at 2000 rpm at an acceleration of 100 rpm/s.

Self-assembly of the PL molecule: 35.0 mg of coumarin derivative **6** were dissolved in 1 mL EtOH (0.07 M solution). The prepared round glass slides with either SiO_2–IOs or mesoporous silica films were placed in a beaker in an elevated and horizontal position and were covered with the coumarin solution by adding two drops of it. The glass slides were left to dry at room temperature. After 5 min, the solvent was evaporated, and this procedure was repeated two times. The glass slides were brought into a vertical position and were washed with EtOH (3x2 mL) and left to dry for 1 h.

Assembly of bulk macro-mesoporous SiO_2–IOs for catalysis: 81 mL (4.5 wt%) PS particles with a diameter of 370 nm (polydispersity index $p = 0.04$), prepared by emulsion polymerization[82] were mixed with 9.9 mL (30 wt%) SiO_2 NPs with a diameter of 10 nm (PlasmaChem). The particle suspension was let to assemble in a mixed colloidal crystal via gravimetrical sedimentation at room temperature. The PS template was removed by pyrolysis in air at 450 °C for 3 hours (1 °C/min), and the corresponding macro-mesoporous SiO_2–IO structure was formed.

Immobilization of 3-azidopropyl triethoxysilane in bulk macro-mesoporous SiO_2–IO: 300 mg SiO_2–O was placed in SAM solution consisting of 200 μL 3-azidopropyl triethoxysilane (AzPTES), 200 μL triethylamine and 1 mL toluene and left to immobilize for 48 hours. After removal of the SAM solution, the functionalized SiO_2–IO was cleaned from the residual, not immobilized silane via multiple washing steps including stirring in toluene and solvent separation via centrifugation (1 min, 5000 rpm).

Characterization methods: SiO_2–IOs and the reference mesoporous silica were imaged by a Zeiss Merlin SEM at 1.7 kV. The samples were sputtered with 5 nm Ir. ICP-OES analysis of immobilized with AzPTES SiO_2–IO was performed on a Spectro CIROS instrument. The quantity of N and C was determined to calculate the amount of the silane molecules attached in the porous silica. Spin-coating experiments were performed on a Laurell WS-650 spin coater. BET measurements were performed at 77 K using a Quantachrome Autosorb 3B instrument. Confocal Laser Scanning Microscopy (CLSM) was performed on a commercial device, LSM 880 (Carl Zeiss, Jena, Germany). The excitation was done with a diode laser (LDH-D-C-405, PicoQuant, Berlin, Germany) operating at 402 nm and focused into the studied samples through a C-Apochromat 40x/1.2 W water immersion objective (Carl Zeiss, Jena, Germany). The emission was collected with the same objective and after passing through a confocal pinhole (set to 1 Airy unit), directed to a spectral detection unit (Quasar, Carl Zeiss) in which a detection range 410–520 nm was selected. Series of images (z-stacks) from optical sections positioned at different distances from the cover glass/inverse opal interface were collected by continuously shifting the microscope objective with a step of 0.5 μm (using a stepper motor).

From these images, 3D reconstructions of the studied IOs were prepared. The bulk SiO_2 inverse replica used for catalysis was analyzed by SAXS at the XEUSS SAXS/WAXS system from Xenocs. The instrument is equipped with a CuKα source ($\lambda = 1.541$ Å, GeniX ultra low divergence, Xenocs) and a Pilatus 300 K hybrid pixel detector (Dectris). A powder of the SiO_2 inverse opal was captured between two Kapton® stripes of 1 mm thickness in a home-built cell holder. The measurement was performed at room temperature and a sample-to-detector distances of 2.7 m and 0.8 m, which allowed to investigate a q-range of 0.005–0.482 Å^{-1}, where $q = 4\pi \sin(\theta/2)/\lambda$ is the absolute value of the scattering vector and q the scattering angle. The raw data treatment was performed using the evaluation software Foxtrot assuming a close-packed packing and considering the measurement time, the transmission, and the background scattering. Finally, the data was normalized using glassy carbon type 2[83] as standard. However, due to the inhomogeneous packing of the powder in the sample holder, the sample volume is error-prone. Therefore, the scattering intensity is given in arbitrary units. The analysis of the scattering data was performed using SASfit version 0.94.11. In order to describe the low q-region Porod's q^{-4} decay[69] was used, whereas for the scattering curve at intermediate and large q- values, dominated by the scattering contributions of the SiO_2 NPs, we chose the form factor for polydisperse spheres[84] with a gaussian size distribution combined with the Percus-Yevick hard sphere structure factor[85] and the local monodisperse approximation.[86]

Acknowledgements

Generous financial support by the Deutsche Forschungsgemeinschaft DFG (grant numbers 358283783 – SFB 1333, subprojects A5, A7, B3) is gratefully acknowledged. The authors would like to thank Tim Julian Stank from the group of Prof. Thomas Hellweg at the University of Bielefeld for performing the SAXS measurements. Open access funding enabled and organized by Projekt DEAL.

Conflict of Interest

The authors declare no conflict of interest.

Keywords: asymmetric heterogeneous catalysis · confocal laser scanning microscopy · diene ligands · rhodium · silica inverse opals

[1] W. Liu, A. Wang, J. Tang, S.-L. Chen, G. Yuan, K. Zhao, C. Li, X. Liu, *Microporous Mesoporous Mater.* **2015**, *204*, 143–148.
[2] A. A. Voskanyan, K.-Y. Chan, C.-Y. V. Li, *Chem. Mater.* **2016**, *28*, 2768–2775.
[3] G. I. N. Waterhouse, W.-T. Chen, A. Chan, H. Jin, D. Sun-Waterhouse, B. C. C. Cowie, *J. Phys. Chem. C* **2015**, *119*, 6647–6659.
[4] G. I. N. Waterhouse, W.-T. Chen, A. Chan, D. Sun-Waterhouse, *ACS Omega* **2018**, *3*, 9658–9674.
[5] T. K. Rahul, N. Sandhyarani, *ChemNanoMat* **2018**, *4*, 642–648.
[6] C. Yang, Q. Li, *J. Photochem. Photobiol. A* **2019**, *371*, 118–127.
[7] G. Collins, M. Blömker, M. Osiak, J. D. Holmes, M. Bredol, C. O'Dwyer, *Chem. Mater.* **2013**, *25*, 4312–4320.
[8] C. Lv, X. Lan, L. Wang, Q. Yu, M. Zhang, H. Sun, J. Shi, *Catal. Sci. Technol.* **2019**, *9*, 6124–6135.
[9] F. Sordello, C. Minero, *Appl. Catal. B* **2015**, *163*, 452–458.
[10] V. Dusastre, *Nat. Mater.* **2013**, *12*, 1080–1080.
[11] X. Huang, W. Gu, S. Hu, Y. Hu, L. Zhou, J. Lei, L. Wang, Y. Liu, J. Zhang, *Catal. Sci. Technol.* **2020**, *10*, 3694–3700.
[12] G. Guan, R. Zapf, G. Kolb, V. Hessel, H. Löwe, J. Ye, R. Zentel, *Int. J. Hydrogen Energy* **2008**, *33*, 797–801.
[13] Y. Tian, L. Zhou, Q. Zhu, J. Lei, L. Wang, J. Zhang, Y. Liu, *Nanoscale* **2019**, *11*, 20638–20647.
[14] B. Chen, L. Zhou, Y. Tian, J. Yu, J. Lei, L. Wang, Y. Liu, J. Zhang, *Phys. Chem. Chem. Phys.* **2019**, *21*, 12818–12825.
[15] Y. Zhao, B. Yang, J. Xu, Z. Fu, M. Wu, F. Li, *Thin Solid Films* **2012**, *520*, 3515–3522.
[16] J. Xu, B. Yang, M. Wu, Z. Fu, Y. Lv, Y. Zhao, *J. Phys. Chem. C* **2010**, *114*, 15251–15259.
[17] F. Li, X. Zhao, J. Mahmood, M. S. Okyay, S.-M. Jung, I. Ahmad, S.-J. Kim, G.-F. Han, N. Park, J.-B. Baek, *ACS Nano* **2017**, *11*, 7527–7533.
[18] S. Zhang, H.-M. Kwon, Z. Li, A. Ikoma, K. Dokko, M. Watanabe, *ChemElectroChem* **2015**, *2*, 1207–1207.
[19] Y. Zhao, Y. Guo, X. Wang, X. Zhang, *J. Mater. Sci.* **2020**, *55*, 2006–2017.
[20] Y. Jiang, P. Zheng, D. Li, L. Zhou, L. Tian, J. Wang, B. Yang, X. Wang, X. Zhang, J. Gao, *Biochem. Eng. J.* **2016**, *112*, 123–129.
[21] B. Zhao, L. Zhou, L. Ma, Y. He, J. Gao, D. Li, Y. Jiang, *Int. J. Biol. Macromol.* **2018**, *107*, 2034–2043.
[22] D. B. Gornowich, G. J. Blanchard, *J. Phys. Chem. C* **2012**, *116*, 12165–12171.
[23] Y. Jiang, P. Zheng, L. Zhou, W. Kong, J. Gao, J. Wang, J. Gu, X. Zhang, X. Wang, *J. Mol. Catal. B* **2016**, *130*, 96–103.
[24] X. Fang, K. P. Sokol, N. Heidary, T. A. Kandiel, J. Z. Zhang, E. Reisner, *Nano Lett.* **2019**, *19*, 1844–1850.
[25] S. Y. Lee, K. Y. Choi, *Ind. Eng. Chem. Res.* **2012**, *51*, 9742–9749.
[26] T. Cherdhirankorn, M. Retsch, U. Jonas, H.-J. Butt, K. Koynov, *Langmuir* **2010**, *26*, 10141–10146.
[27] R. Raccis, A. Nikoubashman, M. Retsch, U. Jonas, K. Koynov, H.-J. Butt, C. N. Likos, G. Fytas, *ACS Nano* **2011**, *5*, 4607–4616.
[28] J. Xie, M. Doroshenko, U. Jonas, H.-J. Butt, K. Koynov, *ACS Macro Lett.* **2016**, *5*, 190–194.
[29] E. B. Anderson, M. R. Buchmeiser, *ChemCatChem* **2012**, *4*, 30–44.
[30] A. E. Fernandes, A. M. Jonas, O. Riant, *Tetrahedron* **2014**, *70*, 1709.
[31] Y. Li, C. Cai, *Chem. Asian J.* **2011**, *6*, 2592–2605.
[32] J. H. Park, Y. Jung, Y. Yang, H. S. Shin, S. Kwon, *ACS Appl. Mater. Interfaces* **2016**, *8*, 25915–25922.
[33] Y. Heo, H. Kang, J.-S. Lee, Y.-K. Oh, S.-H. Kim, *Small* **2016**, *12*, 3819–3826.
[34] F. Ziegler, J. Teske, I. Elser, M. Dyballa, W. Frey, H. Kraus, N. Hansen, J. Rybka, U. Tallarek, M. R. Buchmeiser, *J. Am. Chem. Soc.* **2019**, *141*, 19014–19022.
[35] Z. Feng, J. Zhong, W. Guan, R. Tian, C. Lu, C. Ding, *Analyst* **2018**, *143*, 2090–2095.
[36] C. Li, W. Wang, X. Wang, H. Jiang, J. Zhu, S. Lin, *Eur. Polym. J.* **2015**, *68*, 409–418.
[37] H. Xu, B. Dong, Q. Xiao, X. Sun, X. Zhang, J. Lyu, Y. Yang, L. Xu, X. Bai, S. Zhang, H. Song, *ACS Appl. Mater. Interfaces* **2017**, *9*, 30510–30518.
[38] A. V. Kubarev, K. P. F. Janssen, M. B. J. Roeffaers, *ChemCatChem* **2015**, *7*, 3646–3650.
[39] Y. Jiang, W. Sun, Y. Wang, L. Wang, L. Zhou, J. Gao, Y. He, L. Ma, X. Zhang, *Enzyme Microb. Technol.* **2017**, *96*, 42–46.
[40] T. Hayashi, K. Ueyama, N. Tokunaga, K. Yoshida, *J. Am. Chem. Soc.* **2003**, *125*, 11508–11509.
[41] C. Defieber, H. Grützmacher, E. M. Carreira, *Angew. Chem. Int. Ed.* **2008**, *47*, 4482–4502; *Angew. Chem.* **2008**, *120*, 4558–4579.
[42] J. B. Johnson, T. Rovis, *Angew. Chem. Int. Ed.* **2008**, *47*, 840–871; *Angew. Chem.* **2008**, *120*, 852–884.
[43] M. Nagamoto, T. Nishimura, *ACS Catal.* **2017**, *7*, 833–847.
[44] H. Miyamura, T. Yasukawa, Z. Zhu, S. Kobayashi, *Adv. Synth. Catal.* **2020**, *362*, 353–359.
[45] T. Kuremoto, T. Yasukawa, S. Kobayashi, *Adv. Synth. Catal.* **2019**, *361*, 3698–3703.
[46] H. Min, H. Miyamura, T. Yasukawa, S. Kobayashi, *Chem. Sci.* **2019**, *10*, 7619–7626.
[47] G. Shen, T. Osako, M. Nagaosa, Y. Uozumi, *J. Org. Chem.* **2018**, *83*, 7380–7387.
[48] H. Miyamura, K. Nishino, T. Yasukawa, S. Kobayashi, *Chem. Sci.* **2017**, *8*, 8362–8372.
[49] T. Yasukawa, H. Miyamura, S. Kobayashi, *Chem. Sci.* **2015**, *6*, 6224–6229.
[50] H. Yang, M. Xu, *Chin. J. Chem.* **2013**, *31*, 119–122.
[51] S. S. Garg, J. Gupta, S. Sharma, D. Sahu, *Eur. J. Pharm. Sci.* **2020**, *152*, 105424.

[52] G. Tian, Z. Zhang, H. Li, D. Li, X. Wang, C. Qin, *Crit. Rev. Anal. Chem.* **2020**, *0*, 1–17.
[53] X. Sun, T. Liu, J. Sun, X. Wang, *RSC Adv.* **2020**, *10*, 10826–10847.
[54] M. M. Heravi, S. Khaghaninejad, M. Mostofi, *Adv. Heterocycl. Chem.* (Ed.: A. R. Katritzky), Academic Press, New York, **2014**, pp. 1–50.
[55] M. Tasior, D. Kim, S. Singha, M. Krzeszewski, K. Han Ahn, D. T. Gryko, *J. Mater. Chem. C* **2015**, *3*, 1421–1446.
[56] R. H. Vekariya, H. D. Patel, *Synth. Commun.* **2014**, *44*, 2756–2788.
[57] M. Kirchhof, K. Gugeler, F. Fischer, M. Nowakowski, A. Bauer, S. Álvarez-Barcia, K. Abitaev, M Schnierle, Y Qawasmi, W. Frey, A. Baro, D. Estes, T. Sottmann, M Ringenberg, B. Plietker, M. Bauer, J. Kästner, S. Laschat, *Organometallics* **2020**, 39, 3131–3145.
[58] F. Xue, Q. Liu, Y. Zhu, Y. Qing, B. Wan, *RSC Adv.* **2019**, *9*, 25377–25381.
[59] T. Mühlhäuser, A. Savin, W. Frey, A. Baro, A. J. Schneider, H.-G. Döteberg, F. Bauer, A. Köhn, S. Laschat, *J. Org. Chem.* **2017**, *82*, 13468–13480.
[60] N. Sieffert, J. Boisson, S. Py, *Chem. Eur. J.* **2015**, *21*, 9753–9768.
[61] C. Defieber, J.-F. Paquin, S. Serna, E. M. Carreira, *Org. Lett.* **2004**, *6*, 3873–3876.
[62] E. J. Eisenbraun, *Org. Synth.* **1965**, *45*, 28.
[63] W. Phakhodee, C. Duangkamol, D. Yamano, M. Pattarawarapan, *Synlett* **2017**, *28*, 825–830.
[64] K. C. Nicolaou, D. Rhoades, Y. Wang, R. Bai, E. Hamel, M. Aujay, J. Sandoval, J. Gavrilyuk, *J. Am. Chem. Soc.* **2017**, *139*, 7318–7334.
[65] A. T. Johnson, L. Wang, A. M. Standeven, M. Escobar, R. A. S. Chandraratna, *Bioorg. Med. Chem.* **1999**, *7*, 1321–1338.
[66] P. Wang, Y. Fang, J. Jiang, Y. Ji, Y. Li, J. Zheng, Q. Xu, J. Lu, *Chem. Asian J.* **2017**, *12*, 1790–1795.
[67] G. Singh, S. S. Mangat, J. Singh, A. Arora, R. K. Sharma, *Tetrahedron Lett.* **2014**, *55*, 903–909.
[68] A. Galukhin, D. Bolmatenkov, A. Emelianova, I. Zharov, G. Y. Gor, *Langmuir* **2019**, *35*, 2230–2235.
[69] G. Porod, *Small-Angle X-Ray Scattering*, Determination of General Parameters by Small-Angle X-Ray Scattering. (Ed.: H. Brumberger), Gordon & Breach, New York, London and Paris, **1967**; pp 1–15.
[70] S. Helbig, S. Sauer, N. Cramer, S. Laschat, A. Baro, W. Frey, *Adv. Synth. Catal.* **2007**, *349*, 2331–2337.
[71] M. Deimling, M. Kirchhof, B. Schwager, Y. Qawasmi, A. Savin, T. Mühlhäuser, W. Frey, B. Claasen, A. Baro, T. Sottmann, S. Laschat, *Chem. Eur. J.* **2019**, *25*, 9464–9476.
[72] C.-Y. Wu, Y.-N. Yu, M.-H. Xu, *Org. Lett.* **2017**, *19*, 384–387.
[73] X.-S. Tu, N.-N. Zeng, R.-Y. Li, Y.-Q. Zhao, D.-Z. Xie, Q. Peng, X.-C. Wang, *Angew. Chem. Int. Ed.* **2018**, *57*, 15096–15100.
[74] S.-S. Zhang, T.-J. Hu, M.-Y. Li, Y.-K. Song, X.-D. Yang, C.-G. Feng, G.-Q. Lin, *Angew. Chem. Int. Ed.* **2019**, *58*, 3387–3391.
[75] X.-W. Qian, Z.-J. Xue, Q. Zhao, Z. Cui, Y.-J. Chen, C.-G. Feng, G.-Q. Lin, *Org. Lett.* **2017**, *19*, 5601–5604.
[76] D. Chen, D.-X. Zhu, M.-H. Xu, *J. Am. Chem. Soc.* **2016**, *138*, 1498–1501.
[77] C.-G. Feng, Z.-Q. Wang, P. Tian, M.-H. Xu, G.-Q. Lin, *Chem. Asian J.* **2008**, *3*, 1511–1516.
[78] T. Farooq, L. K. Sydnes, K. W. Törnroos, B. E. Haug, *Synthesis* **2012**, *44*, 2070–2078.
[79] L. Li, T. Shang, X. Ma, H. Guo, A. Zhu, G. Zhang, *Synlett* **2015**, *26*, 695–699.
[80] E. A. B. Kantchev, *Chem. Sci.* **2013**, *4*, 1864–1875.
[81] H. Duan, S. Sengupta, J. L. Petersen, X. Shi, *Organometallics* **2009**, *28*, 2352–2355.
[82] K. Abitaev, Y. Qawasmi, P. Atanasova, C. Dargel, J. Bill, T. Hellweg, T. Sottmann, *Colloid Polym. Sci.* **2021**, 299, 243–258.
[83] F. Zhang, J. Ilavsky, G. G. Long, J. P. G. Quintana, A. J. Allen, P. R. Jemian, *Metall. Mater. Trans. A* **2010**, *41*, 1151–1158.
[84] A. Guinier, G. Fournet, *Small-Angle Scattering of X-Rays*, Wiley, **1955**.
[85] J. K. Percus, G. J. Yevick, *Phys. Rev.* **1958**, *110*, 1–13.
[86] J. S. Pedersen, *J. Appl. Crystallogr.* **1994**, *27*, 595–608.

Manuscript received: December 16, 2020
Revised manuscript received: February 10, 2021
Accepted manuscript online: February 28, 2021
Version of record online: ■■, ■■■

FULL PAPERS

Molecular infiltration: Spatial distribution and tethering sites of catalyst-resembling probe molecules in macro-mesopores silica inverse opal (SiO_2–IO) films were studied via confocal laser scanning microscopy. Bulk macro-mesoporous SiO_2–IOs were further used for attachment of mono- and bis-functionalized chiral Rh diene complexes, and the catalytic activity and selectivity with respect to the porous material was studied in the asymmetric 1,2-addition to *N*-tosylimines.